

Enhanced detection of circularly polarized photons with topological materials

Hamideh Sharifpour^{1,*} George de Coster^{2,3,†} and Avik W. Ghosh^{1,‡}

¹*Department of Electrical and Computer Engineering,
University of Virginia, Charlottesville, VA, 22904, USA*

²*DEVCOM Army Research Laboratory, 2800 Powder Mill Road, Adelphi, MD, 20738 USA*

³*MIT Institute for Soldier Nanotechnologies, 500 Technology Square, Cambridge, MA, 02139, USA*
(Dated: January 30, 2026)

Topological insulators (TI) are highly attractive platforms for next-generation optoelectronic and photonic devices. Spin-momentum locking of topological surface states enhance their nonlinear optical responses and sensitivities, especially to circularly polarized light. Until now, theoretical investigations of nonlinear responses in TIs have been limited to microscopic calculations on analytical continuum models, or leveraging density functional theory based Hamiltonians. In this work, we expand beyond these two approaches by employing a nonlinear Kubo formalism to calculate second-order nonlinear optical conductivity in a slab geometry using symmetry informed tight binding models that accurately reproduce the conduction, valence and topological surface bands in Bi_2Se_3 . Our methodology enables us to study the layer resolved contribution to injection-currents coupled to the incident electric field. We demonstrate that our technique can reveal how device engineering modifies elements of the nonlinear optical response such as the circular photogalvanic effect by breaking inversion and time-reversal symmetry. We find, in line with experiments, that the photogalvanic current is sensitive to field effects, Fermi level energy, gate voltage and the energy of incident light. Our computed midwavelength infrared (mid-IR) responsivity $R \approx 0.169 \mu\text{A}/\text{W}$ is comparable to reported TI and intrinsic 2D-material photodetectors. We further simulate experimentally unexplored methods to modify the circular photogalvanic effect such as proximitizing a magnetic field to one of the TI surface materials, suggesting a mechanism for optoelectronic tuning.

I. INTRODUCTION

Quantum materials serve as a rich platform for exploring unconventional transport and optical properties [1–3]. In particular, topological insulators (TIs) are characterized by an insulating bulk with robust metallic surface states protected by time-reversal symmetry, generating an extensive landscape to explore fundamental physical principles and engineer next-generation optoelectronic devices [4, 5]. The surface states of TIs are topologically distinct, featuring spin-momentum locking and a Dirac-like energy spectrum, which enables exotic responses to external electromagnetic fields [6]. Among known TIs, bismuth selenide (Bi_2Se_3) has emerged as a model system due to its relatively simple electronic structure and modest bulk band gap, which allows for the experimental isolation of its surface states [7]. Other compounds such as Bi_2Te_3 , Sb_2Te_3 , and their doped or alloyed analogs contribute to the family of three-dimensional TIs, all together offering unprecedented control over their electronic and optical properties [8].

Linear and nonlinear optical processes describe fundamentally distinct regimes of light-matter interactions, both relevant to TIs, particularly at their boundaries [9]. In the linear optical regime, the material response is directly proportional to the applied electric field \mathbf{E} , expressed as: $\mathbf{P} = \epsilon_0 \chi^{(1)} \mathbf{E}$, where ϵ_0 is the

vacuum permittivity and $\chi^{(1)}$ is the linear susceptibility [10]. Conversely, nonlinear optical effects arise at high light intensities, where the response exceeds linearity, and higher-order terms contribute to polarization: $\mathbf{P} = \epsilon_0 (\chi^{(1)} \mathbf{E} + \chi^{(2)} \mathbf{E}^2 + \chi^{(3)} \mathbf{E}^3 + \dots)$, where $\chi^{(2)}$ and $\chi^{(3)}$ are the second- and third-order nonlinear susceptibilities, respectively[11]. These nonlinear contributions enable phenomena such as SHG, third-harmonic generation (THG) and sum- and difference-frequency generation. For example, second-harmonic generation (SHG) involves two photons at frequency ω combining to produce a new photon at 2ω [12]. Similarly, the current density \mathbf{J} , linked to optical conductivity, expands as:

$$\mathbf{J} = \sigma^{(1)} \mathbf{E} + \sigma^{(2)} \mathbf{E}^2 + \sigma^{(3)} \mathbf{E}^3 + \dots, \quad (1)$$

where $\sigma^{(n)}$ denotes the n -th order optical conductivity [13]. Unlike linear responses, higher-order components of the current can be generated under intense or structured light excitation, facilitating advanced processes like harmonic generation, optical rectification, and photovoltaic currents beyond conventional limits [14].

A major nonlinear effect in TIs is referred to as the photogalvanic effect (PGE), in which light generates a non-zero current with no applied bias [15–19]. This effect originates from the lack of inversion symmetry, which induces asymmetric optical transitions in the electronic band structure and gives rise to a directional nonlinear optical response [20]. There are two sub-classifications of PGE: the circular photogalvanic effect (CPGE), which is sensitive to the helicity of circularly polarized light, and the linear photogalvanic effect (LPGE), driven by linearly polarized light in response to an anisotropic optical trans-

* avz6gh@virginia.edu

† george.j.decoster.civ@army.mil

‡ ag7rq@virginia.edu

sition [21]. Of the two effects, the CPGE serves not only as a probe of hidden symmetries and topological properties, but also provides a direct insight into the Berry curvature and spin textures in momentum space [22, 23]. The presence of spin-momentum locking in TIs naturally favors CPGE - an isolated up (down) spin electron preferentially couples to right (left) circularly polarized light. However, due to symmetric distribution of states in their \vec{k} -space over which the current integrates, a chiral photon cannot produce a net momentum flow in a centrosymmetric Dirac cone through a linear optical process. In addition, while DC current density breaks time-reversal symmetry, linear photoabsorption does not, which is why we need to look at nonlinear response to seek out signatures of chirality.

Importantly, when inversion symmetry is broken, either intrinsically via structural modifications or extrinsically through applied fields or interfaces, CPGE signals can be significantly enhanced, making TIs with broken symmetries particularly appealing candidates for realizing chiral photodetectors and polarization-sensitive devices [24].

In this work, we attempt a complete description of nonlinear helical photocurrents in topological materials by explicitly calculating the injection current from the second-order optical conductivity tensor $\sigma_{\mu\alpha\beta}^{(2)}(\omega)$. Physically, this represents a population imbalance in momentum-space generated by the optical field [17]. Another second-order response is the shift current, which, unlike the injection current, is caused by a real-space displacement of the wavepacket center during interband optical transitions [25]. We construct a theoretical framework to explain nonlinear optical conductivity in three-dimensional TIs based on a slab Hamiltonian. Unlike previous works employing continuum models within Fermi's golden rule and the Boltzmann equation, this method inherently includes bulk and surface states and thereby all interband transitions [16, 23]. In this manner we can solve layer-resolved contributions to CPGE and LPGE. We analyze the effects of inversion-symmetry breaking—induced by gating, finite slab thickness, and their corresponding electric-field profiles—on the magnitude and character of the photocurrents. We find that the nonlinear photocurrent response in TIs is strongly dependent on the gate voltage, the Fermi level, the incident light frequency and magnetic proximity. Notably, we investigate the effect of magnetization on CPGE, by including in our model a ferromagnetic layer deposited on the TI. We discover that breaking time-reversal and inversion symmetry by this top layer magnet provides an additional knob that can be tuned to boost, suppress, or even reverse helicity-dependent photocurrents, through a redistribution of Berry curvature from inside the magnetic gap to right above the edges.

Our treatment, which separates out bulk, surface and interlayer contributions, is in line with recent experiments shown in Fig.6, and provides an approach towards production of next-generation quantum and chiral-

sensitive optoelectronic devices working in the terahertz to mid-infrared regime.

II. THEORETICAL MODEL AND METHODOLOGY

A. Tight Binding Model

We employ a lattice-regularized effective Hamiltonian to describe a three-dimensional TI [26–28]. The system is modeled as a slab geometry comprising atomic layers stacked along the z -direction. This has the desired effect of inherently containing the bulk and topological surface states so that the interband transitions from surface to bulk states which underlie CPGE and LPGE in Bi_2Se_3 are captured *a priori*. The approach eliminates the need to explicitly solve for the bulk and surface wavefunctions in the continuum model or to include each set of transitions manually [16, 23, 29].

The low-energy Hamiltonian for in-plane momentum components k_x and k_y is expressed in a $4N_z \times 4N_z$ matrix form as:

$$\mathcal{H} = \mathbf{c}^\dagger(\mathbf{k}) H_{\text{tot}} \mathbf{c}(\mathbf{k}), \quad (2)$$

$$H_{\text{tot}} = H_0 \otimes \mathbb{1}_{4N_z \times 4N_z} + H_z, \quad (3)$$

where H_0 is the in-plane on-site Hamiltonian, \otimes represents a tensor product, and H_z encodes interlayer coupling terms. The ladder operators $c_{z,s}(\mathbf{k})$ are $4N_z$ dimensional vectors Fourier transformed in the 2D-plane (i.e. $\mathbf{k} = (k_x, k_y)$). The Hamiltonian H_{tot} is constructed using Dirac matrices derived from Pauli matrices σ_i . The momentum-dependent on-site Hamiltonian H_0 includes terms capturing lattice symmetries and spin-orbit coupling:

$$H_0(\mathbf{k}) = \varepsilon_0(\mathbf{k}) \mathbb{1}_{4 \times 4} + \sum_{i=1}^5 \varepsilon_i(\mathbf{k}) \Gamma_i, \quad (4)$$

where $\varepsilon_i(\mathbf{k})$ are scalar functions encoding energy dispersions, and the 4×4 Dirac matrices Γ_i are defined as:

$$\begin{aligned} \Gamma_1 &= \sigma_x \otimes \tau_x, & \Gamma_2 &= \sigma_y \otimes \sigma_x, & \Gamma_3 &= \sigma_z \otimes \sigma_x, \\ \Gamma_4 &= I_2 \otimes \sigma_y, & \Gamma_5 &= I_2 \otimes \sigma_z. \end{aligned} \quad (5)$$

Here, $\sigma_{x,y,z}$ are the Pauli matrices, and I_2 is the 2×2

identity matrix. The explicit energy terms are:

$$\begin{aligned}\varepsilon_0(\mathbf{k}) &= 2A_0 \sum_{j=1}^3 \cos(\mathbf{k} \cdot \mathbf{a}_j) - 6A_0, \\ \varepsilon_1(\mathbf{k}) &= -2A_{14} \sin \Omega \left[\sin(\mathbf{k} \cdot \mathbf{a}_2) - \sin(\mathbf{k} \cdot \mathbf{a}_3) \right], \\ \varepsilon_2(\mathbf{k}) &= -2A_{14} \left[\sin(\mathbf{k} \cdot \mathbf{a}_1) \right. \\ &\quad \left. + \cos \Omega (\sin(\mathbf{k} \cdot \mathbf{a}_2) + \sin(\mathbf{k} \cdot \mathbf{a}_3)) \right], \\ \varepsilon_3(\mathbf{k}) &= 2A_{12} \sum_{j=1}^3 \sin(\mathbf{k} \cdot \mathbf{a}_j), \\ \varepsilon_4(\mathbf{k}) &= 0, \\ \varepsilon_5(\mathbf{k}) &= 2A_{11} \sum_{j=1}^3 \cos(\mathbf{k} \cdot \mathbf{a}_j) + m_{11}.\end{aligned}$$

The in-plane lattice vectors for the van der Waals planes (Fig. 1) are:

$$\begin{aligned}\mathbf{a}_1 &= (a, 0, 0), \quad a_2 = \left(-\frac{a}{2}, \frac{\sqrt{3}a}{2}, 0 \right), \\ \mathbf{a}_3 &= \left(-\frac{a}{2}, -\frac{\sqrt{3}a}{2}, 0 \right)\end{aligned}\quad (6)$$

and $\Omega = -\frac{2\pi}{3}$ is a geometric parameter representing the relative phase between hopping channels associated with the 120° angle-separated vectors $\tilde{a}_{2,3}$. A_0 , A_{11} , A_{12} , and A_{14} are material-dependent parameters describing hopping strengths and mass terms. The interlayer coupling Hamiltonian between neighboring layers is given by:

$$\begin{aligned}H_z &= \begin{pmatrix} 0 & t_z & & \\ t_z^\dagger & \ddots & \ddots & \\ & \ddots & \ddots & t_z \\ & & t_z^\dagger & 0 \end{pmatrix} \\ t_z &= t_0 I_4 + \sum_{i=1}^5 t_i \Gamma_i,\end{aligned}\quad (7)$$

where:

$$\begin{aligned}t_0 &= B_0 \sum_{j=1}^3 e^{i\mathbf{k} \cdot \mathbf{b}_j}, \\ t_1 &= -iB_{14} \left(e^{i\mathbf{k} \cdot \mathbf{b}_1} + \cos \Omega [e^{i\mathbf{k} \cdot \mathbf{b}_2} + e^{i\mathbf{k} \cdot \mathbf{b}_3}] \right), \\ t_2 &= iB_{14} \sin \Omega (e^{i\mathbf{k} \cdot \mathbf{b}_2} - e^{i\mathbf{k} \cdot \mathbf{b}_3}), \\ t_3 &= 0, \\ t_4 &= iB_{12} \sum_{j=1}^3 e^{i\mathbf{k} \cdot \mathbf{b}_j}, \\ t_5 &= iB_{11} \sum_{j=1}^3 e^{i\mathbf{k} \cdot \mathbf{b}_j}.\end{aligned}$$

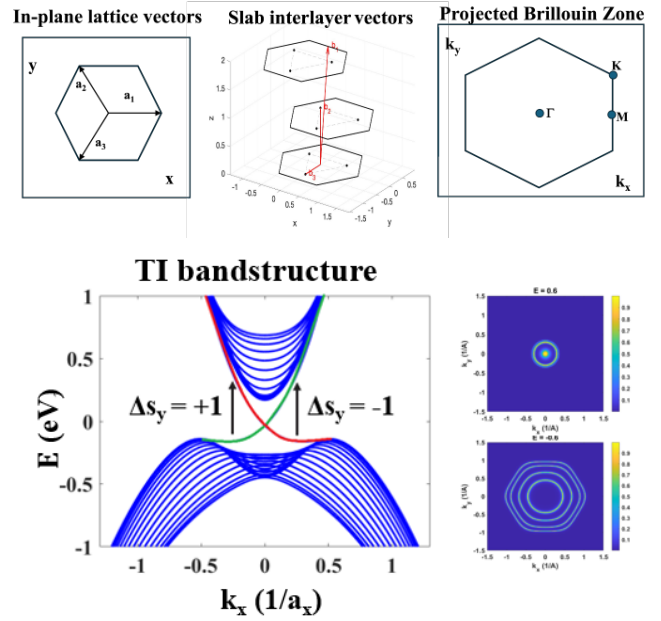


FIG. 1. Top: In-plane lattice unit cell, inter-plane slab vectors, and 2D projection of first Brillouin zone for Bi_2Se_3 . Bottom: Electronic structure of Bi_2Se_3 : slab band structure showing a single Dirac cone bridging the bulk gap, red and green corresponding to y -spin polarization $\langle S_y \rangle = +1$ and -1 respectively. Band structure parameters are fitted to the conduction and valence bands of Bi_2Se_3 ; the constant-energy contours at $E = \pm 0.6$ eV show that warping is only significant in the valence band but insignificant in the conduction band due to the small effective mass of the latter.

The lattice vectors connecting layers in an ABC like rhombohedral packing as in Bi_2Se_3 are (Fig. 1) are:

$$\begin{aligned}\mathbf{b}_1 &= \left(0, \frac{\sqrt{3}a}{2}, c \right), \quad \mathbf{b}_2 = \left(-\frac{a}{2}, -\frac{\sqrt{3}a}{6}, c \right), \\ \mathbf{b}_3 &= \left(\frac{a}{2}, -\frac{\sqrt{3}a}{6}, 0 \right)\end{aligned}\quad (8)$$

with B_0 , B_{11} , B_{12} , and B_{14} describing interlayer hopping and coupling strengths, and c being the lattice constant along the stacking (z) direction. Figure 1 shows the band structure of the TI slab [30] along the high-symmetry $-\bar{M} - \Gamma - \bar{M}$ direction, where the Dirac cone-like topological surface states are evident. Vertical interband transitions to conduction bands are associated with changes in spin orientation ($\Delta S_y = \pm 1$), which enable helicity-selective optical excitation and thus contribute to the CPGE. The spin asymmetry of these transitions is the key mechanism enabling net injection current under circularly polarized illumination. Constant-energy contours in Fig. 1 show weak warpings due to the small conduction band mass of Bi_2Se_3 , evident at $E = 0.6$ eV, while the heavy valence band shows pronounced warping at $E = -0.6$ eV.

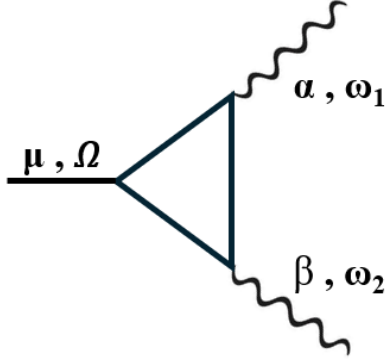


FIG. 2. Diagrammatic representation of the injection current contribution to CPGE: the generated photocurrent $j_\mu(\Omega)$ couples to two optical vertices α, ω_1 and β, ω_2 , giving $j_\mu(\Omega) = \sigma_{\mu\alpha\beta}^\Delta(\omega_1, \omega_2)E_\alpha(\omega_1)E_\beta(\omega_2)$.

B. Nonlinear Optical Conductivity

The second order nonlinear photocurrent is a superposition of Fermi surface, shift and injection current contributions [29]. Together these contributions generate current densities that depend on the stimulating electric field intensity, as well as its optical linear and circular polarizations. Generally, the nonlinear photocurrent j_μ is expressed in terms of the second-order conductivity tensor connecting to the applied optical field components:

$$j_\mu(\Omega) = \sum_{\alpha, \beta} \sigma_{\mu\alpha\beta}(\omega_1, \omega_2)E_\alpha(\omega_1)E_\beta(\omega_2), \quad (9)$$

where $\sigma_{\mu\alpha\beta}$ is the nonlinear optical conductivity tensor and $E_\alpha(\omega_1)$ and $E_\beta(\omega_2)$ are the Fourier components of the electric field. The optical field can be written in real space as [9]:

$$\mathbf{E}(t) = E_0 \hat{e} e^{-i\omega t} + E_0^* \hat{e}^* e^{+i\omega t}, \quad (10)$$

with amplitude E_0 and polarization unit vector \hat{e} . Typically, however, experiments will measure photocurrent j as a function of quarter wave plate angle ϕ that controls

the helicity of light and report photocurrents of the form

$$\frac{j_x}{E_0^2} = C \sin(2\phi) + L_1 \sin(4\phi) + L_2 \cos(4\phi) + D, \quad (11)$$

where the $\sigma_{\mu\alpha\beta}$ elements have been absorbed into the coefficients $C, L_{1,2}$ and D which respectively represent circular polarization, linear polarization, and polarization-independent responses, and ϕ parametrizes the polarization state of light (see derivation in Appendix A and Eq. A6).

In this work, we are primarily interested in the response to circular polarization, which for Dirac states and TIs has been shown to be dominated by the injection current due to spin-momentum locking [31]. Physically, the injection current arises from the asymmetric excitation of carriers into the conduction band, where optical selection rules preferentially populate states at specific crystal momenta. This imbalance produces a net current that grows linearly in time while the light is applied. In the Feynman diagrammatic description, the process is represented by two photon-electron interaction vertices on a single electron propagator [32, 33]. The two field insertions signal the second order character: one interaction promotes an electron from the valence to the conduction band, and the other encodes interference between distinct excitation pathways that generate an asymmetric distribution of conduction-band populations (Fig. 2). In contrast to the shift current, which comes from coherent interband polarization, the injection current reflects a genuine distribution effect, diagrammatically captured by the asymmetric occupation of final states following photon absorption.

Returning to Eq. (11), we would like to identify the tensor elements that correspond to C and $L_{1,2}$ in the case of the circular and linear photogalvanic effect (CPGE and LPGE) respectively. In Appendix A we present the standard symmetry analysis for $\sigma_{\mu\alpha\beta}$ using the C_{3v} point group symmetry for the surface of Bi_2Se_3 , and the fact that for photocurrent generation $\sigma_{\mu\alpha\beta} = \sigma_{\mu\beta\alpha}^*$, to arrive at the simple relations [15, 19, 34]:

$$j_{x,\text{CPGE}} \propto \text{Im } \sigma_{xxz}, \quad j_{x,\text{LPGE}} \propto \text{Re } \sigma_{xxy}.$$

Following previous works to derive the Feynman diagrammatic method of calculating $\sigma_{\mu\alpha\beta}$, we limit ourselves to the injection current represented by the diagram in Fig. 2, and the corresponding restricted conductivity σ^Δ [31, 32, 35]. This diagram is computed as:

$$\begin{aligned} \sigma_{\mu\alpha\beta}^\Delta(\omega_a, \omega_b) = & \frac{-iq^3/\hbar^2}{\pi^2 \omega_{n_1} \omega_{n_2}} \times \\ & \int d\mathbf{k} \sum_{\omega_l} \text{Tr} \left[v_\mu(\mathbf{k}) G(\mathbf{k}, i\omega_l) v_\alpha(\mathbf{k}) G(\mathbf{k}, i\omega_l + i\omega_{n1}) v_\beta(\mathbf{k}) G(\mathbf{k}, i\omega_l + i\omega_{n1} + i\omega_{n2}) \right]_{i\omega_{n1(2)} \rightarrow \omega_{a(b)} + i\delta} \end{aligned} \quad (12)$$

which is equivalent to the Kubo formula presented in previous texts [35]. Here v_α is the velocity operator and $G(\mathbf{k}, i\omega)$ is the matrix Green's function, q is the charge of the electron, \mathbf{k} the absolute value of the momentum, T is

the temperature with $\omega_n = 2n\pi T$ and $\omega_l = (2n + l)\pi T$ the Boson and Fermion Matsubara frequencies, n and l are integers and Tr is a trace. To obtain the nonlinear conductivity, which is a real frequency quantity, we analytically continue from imaginary $i\omega_n$ to real ω , with δ a broadening parameter (for the long wavelength limit $q \rightarrow 0$). In this work we generally assumed $\delta=0.005$ meV. The integral over momentum space is given by $\int d\mathbf{k} = \int dk_x dk_y / 4\pi^2$ for two dimensions (2D). The matrix Green's function $\mathbf{G}(\mathbf{k}, i\omega_l)$ can be conveniently written in terms of the matrix spectral function $\mathbf{A}(\mathbf{k}, \omega)$ as:

$$\mathbf{G}(\mathbf{k}, i\omega_l) = \int_{-\infty}^{\infty} \frac{d\omega}{2\pi} \frac{\mathbf{A}(\mathbf{k}, \omega)}{i\omega_l - \omega} . \quad (13)$$

Using this form of the Green function, we can eliminate the frequency sums in $\sigma_{\alpha\beta\gamma}$ and arrive at the expression:

$$\begin{aligned} \sigma_{\mu\alpha\beta}^{\Delta}(\omega_1, \omega_2) = & \frac{iq^3/\hbar^2}{(\omega_1 + i\delta)(\omega_2 + i\delta)} \times \\ & \int dk \sum_{ijk} \frac{V_{ki}^{\mu} V_{ij}^{\alpha} V_{jk}^{\beta}}{\omega_1 + \omega_2 + i2\delta - E_k(\mathbf{k}) + E_i(\mathbf{k})} \left[\frac{f_D(E_i(\mathbf{k})) - f_D(E_j(\mathbf{k}))}{\omega_1 + i\delta + E_i(\mathbf{k}) - E_j(\mathbf{k})} - \frac{f_D(E_j(\mathbf{k})) - f_D(E_k(\mathbf{k}))}{\omega_2 + i\delta + E_j(\mathbf{k}) - E_k(\mathbf{k})} \right] . \end{aligned} \quad (14)$$

The function $f(\omega)$ represents the Fermi-Dirac distribution, which is given by:

$$f_D(\omega) = \frac{1}{e^{(\omega - E_f)/k_B T} + 1} \quad (15)$$

where E_f is the Fermi level, k_B is the Boltzmann constant, and T is the temperature. The parameters $\omega_{1,2}$ denote incident frequencies, typically related to external perturbations or applied electromagnetic fields. V_{ki}^{α} , V_{ij}^{β} , and V_{jk}^{γ} are matrix elements computed using eigenvectors $|i\rangle$ with eigenvalues $E_i(\mathbf{k})$:

$$V_{ki}^{\alpha} = \langle k | v_{\alpha}(\mathbf{k}) | i \rangle . \quad (16)$$

We use the tight binding model to compute velocity operators in the planar directions $(\mathbf{k}) = (k_x, k_y)$ as:

$$v_{\alpha}(\mathbf{k}) = \frac{\partial H(\mathbf{k})}{\hbar \partial k_{\alpha}} . \quad (17)$$

The real space z -direction of the tight binding model along the growth direction between slab planes requires the z velocity operator to be computed in real space as:

$$v_z(\mathbf{k}) = -\frac{i}{\hbar} [\hat{z}, H(\mathbf{k})] . \quad (18)$$

The z -position operator \hat{z} for the tight binding model acts on the slab layer (i.e. TI quintuple layer). For N_z layers it is the block diagonal matrix:

$$\hat{z} = \begin{pmatrix} 1 & & & \\ & \ddots & & \\ & & N_z & \end{pmatrix} \otimes \mathbb{1}_{4 \times 4} . \quad (19)$$

The expression in Eq. (14) can be written in a much more compact form that better lends itself to numerical

simulation. First, we note that two sets of triangle diagrams with reversed vertices contribute to the injection current, and thus the *effective* injection current conductivity tensor element is:

$$\sigma_{\mu\alpha\beta}^{inj}(\omega_1, \omega_2) \equiv \sigma_{\mu\alpha\beta}^{\Delta}(\omega_1, \omega_2) + \sigma_{\mu\beta\alpha}^{\Delta}(\omega_2, \omega_1) . \quad (20)$$

We define the tensor of eigen-energy differences and Fermi-Dirac occupation differences respectively as $\varepsilon_{mn} = E_m(\mathbf{k}) - E_n(\mathbf{k})$ and $f_{mn} = f_D(E_m(\mathbf{k})) - f_D(E_n(\mathbf{k}))$. We note the sum frequency $\omega = \omega_1 + \omega_2$, suppresses imaginary offsets (i.e. $\omega_1 \equiv \omega_1 + i\delta$), and then construct the tensors

$$\begin{aligned} (t_0^{\mu})_{ij} &= \frac{V_{ij}^{\mu}}{\Omega - \varepsilon_{ij}} , \quad (t_1^{\alpha})_{ij} = \frac{f_{ij} V_{ij}^{\alpha}}{\omega_1 + \varepsilon_{ij}} , \\ (t_2^{\beta})_{ij} &= \frac{f_{ij} V_{ij}^{\beta}}{\omega_2 + \varepsilon_{ij}} . \end{aligned} \quad (21)$$

The effective injection current can then be compactly expressed as:

$$\sigma_{\mu\alpha\beta}^{inj} = i \frac{q^3/\hbar^2}{\omega_1 \omega_2} \text{Tr} \left[t_0^{\mu} \left(t_1^{\alpha} V^{\beta} + t_2^{\beta} V^{\alpha} - V^{\alpha} t_2^{\beta} - V^{\beta} t_1^{\alpha} \right) \right] . \quad (22)$$

Here the Tr operator sums over every degree of freedom such as tensor indices, eigenvalues and momentum.

C. Layer Resolved Injection Current

The inversion symmetry of Bi_2Se_3 guarantees that the second order response tensor is actually zero as $\mathbf{I} : \sigma_{\mu\alpha\beta} \mapsto -\sigma_{\mu\alpha\beta}$ under inversion \mathbf{I} . However, light does not uniformly penetrate a thin film, and a field that decays into the material as $E = E_0 e^{-\lambda z}$ with absorption coefficient λ contributes exponentially diminished weight

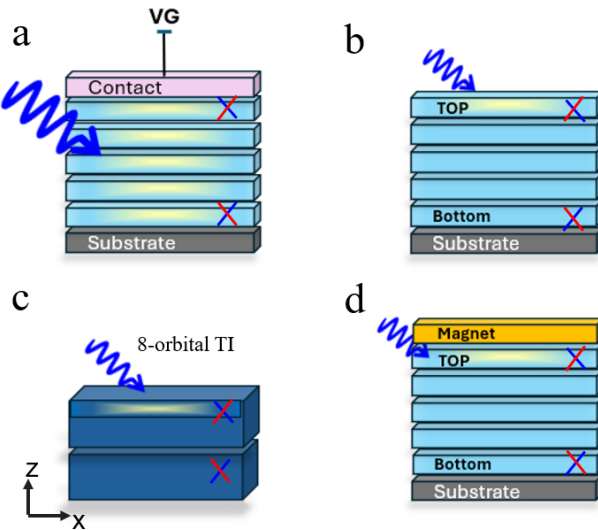


FIG. 3. Schematic of different configurations used to analyze the circular photogalvanic effect (CPGE), ($\text{Im } \sigma_{xxz}$) in TIs. (a) Fully irradiated TI slab, (b) TI surface irradiation, (c) 8-orbital TI, (d) TI slab with a magnetic layer applied to the top surface to break time-reversal symmetry.

to the nonlinear photocurrent at each layer. The vertical optical absorption coefficient in Bi_2Se_3 ranges from $\sim 1/5 \text{ nm}^{-1}$ to $\sim 1/100 \text{ nm}^{-1}$ for visible to long wave infrared light respectively [36]. This implies that for the

typical thin film thicknesses of $\mathcal{O}(10 \text{ nm})$ in nonlinear photocurrent generation studies in Bi_2Se_3 , we can expect the bottom surface to be weighted as little as 13% relative to the top surface. Thin film/substrate interface effects can further hamper the bottom surface's participation in $\sigma_{\mu\alpha\beta}$, so we are motivated to study the layer resolved contributions to the photocurrent [16, 23, 24]. In particular we would like to extract the impact of the top two ($l = 1, 2$) and bottom two layers ($l = N_z - 1, N_z$) to capture the majority of the topological surface state wavefunctions' contribution to $\sigma_{\mu\alpha\beta}^{\text{inj}}$.

We can account for the layer resolved contributions to the injection current by separating layer and spin/orbit degrees of freedom as $l = 1, \dots, N_z$ and $s = 1, 2, 3, 4$. We observe that the velocity tensor $(v_z(\mathbf{k})_{(l_1, s_1), (l_2, s_2)})$ encodes the hopping or 'current' that flows from layer l_2 to l_1 [37, 38]. As we care about the current that flows to a given layer l , we can compute this via left projection

$$\begin{aligned} v_{z,l}(\mathbf{k}) &\equiv P_l \cdot v_z(\mathbf{k}) \\ &= \text{diag}(0, \dots, 0, \underset{\substack{\uparrow \\ l\text{th position}}}{1}, 0, \dots, 0) \otimes \mathbb{1}_{4 \times 4} \cdot v_z(\mathbf{k}), \end{aligned} \quad (23)$$

where only the l th entry of the diagonal matrix is non-zero. By inserting these projectors P_l into our original triangle diagram we can obtain the layer restricted contribution to the injection current:

$$\begin{aligned} \sigma_{\mu\alpha\beta,l}^{\Delta}(\omega_a, \omega_b) &= \frac{-iq^3/\hbar^2}{\pi^2 \omega_{n_1} \omega_{n_2}} \times \\ &\int d\mathbf{k} \sum_{\omega_l} \text{Tr} [v_{\mu}(\mathbf{k}) G(\mathbf{k}, i\omega_l) (P_l v_{\alpha}(\mathbf{k})) G(\mathbf{k}, i\omega_l + i\omega_{n1}) (P_l v_{\beta}(\mathbf{k})) G(\mathbf{k}, i\omega_l + i\omega_{n1} + i\omega_{n2})]_{i\omega_{n1(2)} \rightarrow \omega_{a(b)} + i\delta} . \end{aligned} \quad (24)$$

We note that due to the block tri-diagonal form of $G(\mathbf{k}, i\omega)$ and $v_{\alpha}(\mathbf{k})$ the product of the last two terms in the trace above would be zero if non-identical projection layers were used, and therefore $\sum_l \sigma_{\mu\alpha\beta,l}^{\Delta}(\omega_a, \omega_b) = \sigma_{\mu\alpha\beta}^{\Delta}(\omega_a, \omega_b)$.

As a final step we can conduct analysis identical to the previous subsection to obtain a form like Eq. (22) using layer projected velocity tensors. For later convenience as a last step we define the top and bottom injection conductivity terms in the DC limit ($\omega_1 = \omega + i\delta$, $\omega_2 = -\omega + i\delta$) as

$$\begin{aligned} \sigma_{\mu\alpha\beta}^T(\omega) &\equiv \text{Im } \sigma_{\mu\alpha\beta,1}^{\text{inj}} + \text{Im } \sigma_{\mu\alpha\beta,2}^{\text{inj}}, \\ \sigma_{\mu\alpha\beta}^B(\omega) &\equiv \text{Im } \sigma_{\mu\alpha\beta,N_z-1}^{\text{inj}} + \text{Im } \sigma_{\mu\alpha\beta,N_z}^{\text{inj}} . \end{aligned} \quad (25)$$

III. BULK CALCULATIONS AND FIELD DEPENDENCE

In this section, we analyze the voltage-tunable nonlinear optical response and polarization-resolved photocurrent generation in our TI slab geometry. Previous experimental studies have observed a strong dependence of CPGE to applied voltages in silicon nanowires [39] and TIs [24]. To illustrate the physical mechanism underlying this voltage-tunable photocurrent response, we first consider the case of uniformly optically excited TIs (as might be the case for extremely thin films, or long wave length excitations), where an applied voltage explicitly breaks the inversion symmetry to mimic contact or gating field effects.

When a finite applied potential, V_G , is applied to the system as shown in Fig. 3(a), the slab Hamiltonian ex-

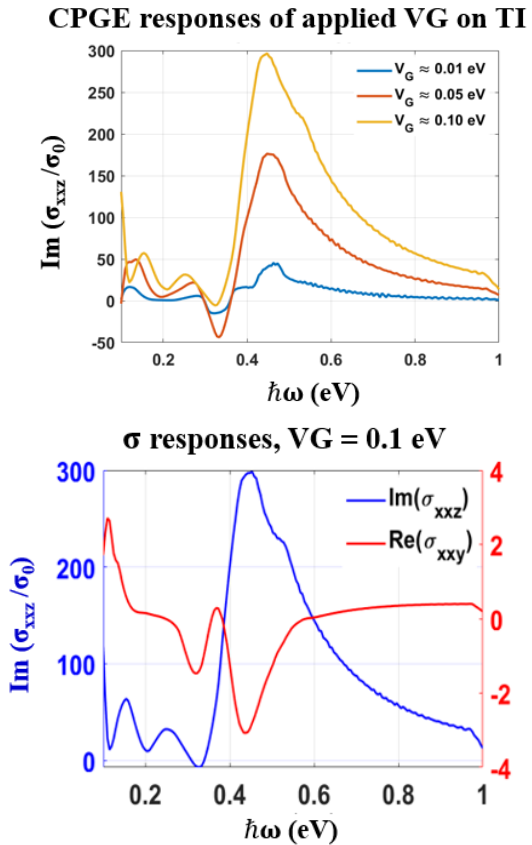


FIG. 4. Top: Imaginary part of the second-order nonlinear optical conductivity component $\text{Im}(\sigma_{xxz})$ of the bulk material (Fig. 3(a)), as a function of photon energy for different applied field strengths. Increasing the field strength from approximately 0.01 to 0.1 results in significant enhancement of the nonlinear optical response, particularly in the 0.4–0.6 eV spectral range. Bottom: comparison of CPGE vs LPGE. Note: $\sigma_0 \approx 6.85 \times 10^{-7} \text{ A/V}^2$.

plicitly breaks inversion symmetry through the layer dependent potential:

$$H_V = \text{diag} \left(-\frac{V_G}{2}, -\frac{(N_z - 1)V_G}{2N_z}, \dots, \frac{V_G}{2} \right) \otimes \mathbb{1}_{4 \times 4} . \quad (26)$$

In this case, the degeneracy of the surface states is lifted and the surface electronic structure is altered as a gap forms (see Fig. B.1). Such behavior is a characteristic of a breaking of the inversion symmetry, as to be expected and especially relevant in fields of optical response under second order, as is the case with the circular photogalvanic effect [39].

To demonstrate the impact on the net nonlinear photocurrent generation, we evaluate the injection conductivity components $\sigma_{xxz}^{\text{inj}}$ and σ_{xy}^{inj} at a Fermi level of $E_f = 0.2$ eV above the Dirac point. This value reflects the typical *n*-type doping of Bi_2Se_3 , where the Fermi level lies within the conduction band due to selenium vacancies, as observed in angle-resolved photoemission

spectroscopy (ARPES) measurements [40].

Figure 4(Top) shows how $\text{Im} \sigma_{xxz}^{\text{inj}}$ increases from 0 as V_G is applied, consistent with $\sigma_{\mu\alpha\beta} \neq 0$ when inversion symmetry is broken. At low applied gate voltages (approximately $V_G \sim 0.01$), the optical transitions are predominantly governed by the intrinsic Dirac-like linear dispersion of the system, resulting in a comparatively weaker nonlinear optical response. The observed peaks in $\text{Im} \sigma_{xxz}$ are attributed to resonant interband transitions that coincide with regions of high density of states and pronounced Berry curvature effects, particularly in the photon energy range of 0.3 to 0.6 eV. Our results clearly demonstrate that the second-order nonlinear optical conductivity component $\text{Im}(\sigma_{xxz})$ exhibits significant resonances with photon energy, whose amplitude and spectral position are highly sensitive to the applied external gate voltage. These resonances originate from field-induced modifications of the band structure, including Dirac cone deformation, band hybridization, and increased asymmetry.

Figure 4(Bottom) illustrates the frequency dependence of injection current contribution to CPGE and LPGE represented by $\text{Im}(\sigma_{xxz})$ and $\text{Re}(\sigma_{xy})$ at $V_G = 0.1$ eV. Injection CPGE is seen to dominate LPGE by two orders of magnitude at this voltage. While both CPGE and LPGE magnitudes grow with V_G , the CPGE response exhibits highly resonant behavior, strongly influenced by the topological band structure and Berry curvature effects. In contrast, the LPGE displays a more gradual spectral evolution, indicative of its dependence on symmetry breaking and anisotropic optical transitions. We recall that $\sigma_{xy} = 0$ for six-fold symmetric band structures, and for weak warping the lower energy bands optically probed by σ_{xy}^{inj} appear effectively six-fold. The warping in our Hamiltonian is controlled by the Hamiltonian parameter A_{ij} . As discussed in Appendix B, by tuning A_{ij} we can account for more pronounced warping like in Bi_2Te_3 to drive up σ_{xy}^{inj} [41].

Our calculations thus far suggest that an applied field controls not only the strength of the photocurrent (shown in Fig. B.2), but also the relative polarization dependencies. Phenomenologically the applied field term H_V can arise due to gating effects or contact field effects, which in both cases have shown to lead to enhanced CPGE to LPGE ratios [16, 39]. Our findings suggest a clear strategy for engineering high-sensitivity photodetection, utilizing resonant frequencies and strong-field-induced nonlinear effects to optimize device performance. The analysis so far has assumed uniform absorption throughout the TI. The next section presents the corresponding layer-resolved calculation, which provides a more complete description.

IV. LAYER-RESOLVED COMPUTATION

A. Four Band Model

In this section, we perform layer-resolved calculations of the injection components of the circular photogalvanic effect (CPGE) in TIs using the slab model in Section II with tight binding parameters corresponding to Bi_2Se_3 as presented in Appendix B and 15 layers. We focus on the imaginary part of the nonlinear injection conductivity, $\text{Im } \sigma_{xxz}^{\text{inj}}(\omega)$, which characterizes the helicity-dependent photocurrent along the x -direction under circularly polarized light. A key property of the slab is that the top and bottom surfaces are related by the mirror symmetry $M_z : (x, y, z) \mapsto (x, y, -z)$, which reverses the surface normal. Because σ_{xxz} carries a single z index, it is odd under inversion:

$$\sigma_{xxz}^{\text{Top}}(\omega) = -\sigma_{xxz}^{\text{Bottom}}(\omega). \quad (27)$$

Thus, the top and bottom surface CPGEs have opposite signs due to their opposite spin-momentum locking and the reversal of velocity matrix elements when the surface normal is inverted. For an inversion-symmetric slab, these contributions cancel. Accordingly, in what follows we report results for a single surface (the top surface); the bottom surface is obtained by an overall sign flip. As mentioned in Section II, in order to capture the majority of the topological surface state wavefunctions, we consider the top two and bottom two layers of the material stack as the ‘surfaces’ in our calculations. In Fig. D.1 (Appendix D) we present $\sigma_{xxz}^{\text{T,B}}(\omega)$ where the top (solid) and bottom (dashed) results for different optical frequencies and Fermi levels are seen to be opposite each other.

Note that in the very low-frequency limit ($\hbar\omega \rightarrow 0$), second-order dc photocurrents are numerically sensitive. Within the length-gauge formalism, the injection (helicity-dependent) contribution involves resonant denominators together with a phenomenological relaxation factor scaling as $1/\delta$. When combined with the Dirac-like dispersion, the resulting integrands become sharply peaked near the Brillouin-zone center and require extremely dense k -meshes and small broadening δ for convergence to zero at $\hbar\omega = 0$. We demonstrate this convergence issue in the Appendix Fig. D.1. To avoid over interpretation of this regime and facilitate large parameter sweeps, all quantitative spectra reported in rest of the main text correspond to $\hbar\omega \geq 0.1$ eV, where the interband-dominated response is well converged with respect to k -mesh, slab thickness, and the relaxation parameter δ .

Figure 5(a) presents a colormap of the calculated $\text{Im } \sigma_{xxz}$ on the top surface as a function of the Fermi level E_f and the photon energy $\hbar\omega$. A pronounced change in the CPGE response is observed across the line $\hbar\omega \sim E_f$, dashed green line, which marks the condition where the photon energy becomes resonant with interband absorption across the Fermi level. The sign reversal

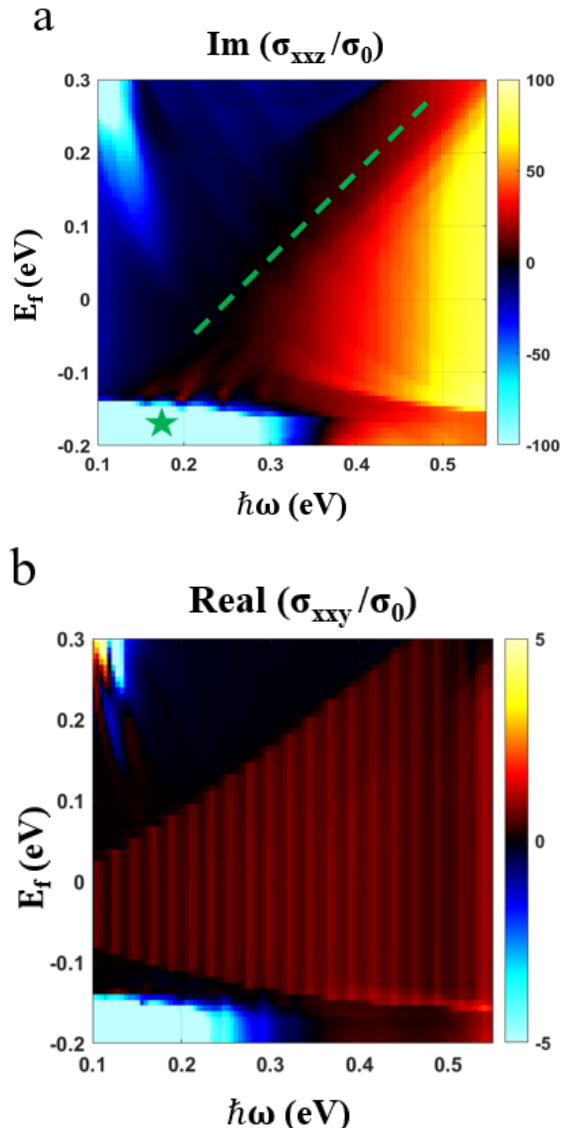


FIG. 5. a) Dependence of top surface layer CPGE $\propto \text{Im}(\sigma_{xxz})$ on Fermi level E_f , and excitation energy, $\hbar\omega$. The surface CPGE flips sign across the green line $E_f = \hbar\omega$. A green star shows that for p-type Bi_2Se_3 , the flattish top of the valence band leads to a large density of states and a corresponding large negative CPGE. b) Plot of LPGE response ($\text{Re}(\sigma_{xxz})$) versus photon energy and Fermi level. LPGE is strongly suppressed relative to CPGE across the parameter space, consistent with surface-cancellation in the slab and the weak in-plane anisotropy of the model. Note: $\sigma_0 \approx 6.85 \times 10^{-7} \text{ A/V}^2$.

of the CPGE across this line indicates a transition from valence-to-conduction to conduction-to-conduction excitation processes, which is consistent with the literature [16]. Further note that there is a finite width to the region where $\sigma_{xxz}^{\text{T}}(\omega \approx E_f)$, which reflects the well known result that intra-Dirac cone excitations yield zero CPGE unless photon drag is included [23, 29]. Once the photon energy is large enough to connect surface and bulk states, then $\sigma_{xxz}^{\text{T}}(\omega \approx E_f)$ increases from zero. This region of zero

conductivity naturally disappears as E_f enters the bulk bands. In the case of p -type Bi_2Se_3 , marked by the green star in Fig. 5(a), the asymmetry in optical excitation is enhanced due to the relatively flat top of the valence band, resulting in a strong negative CPGE response.

Figure 5(b) presents the LPGE response, $\text{Re } \sigma_{xxy}^{\text{inj}}$, as a function of Fermi level E_f and photon energy $\hbar\omega$. Across the entire $(E_f, \hbar\omega)$ range, the LPGE magnitude remains much smaller than the corresponding CPGE response, confirming that it does not influence our main conclusions. The injection-type LPGE channel follows the intrinsic C_{3v} symmetry of the topological surface states and arises mainly from hexagonal warping effects—particularly those affecting the valence band—whose strength is weak within this model. The fringe-like structures observed in $\text{Re } \sigma_{xxy}^{\text{inj}}$ caused by discrete interband transitions between quantized subbands in the finite slab geometry. These features reflect finite-size quantization of surface states, where each stripe corresponds to a resonant transition condition $E_{n,k} - E_{m,k'} = \hbar\omega$, and their modulation by hexagonal warping underscores the symmetry-allowed yet weak nature of the LPGE response.

To evaluate the device performance, we estimate the photoresponsivity arising from the CPGE-induced photocurrent. The calculated responsivity originates from the first two layers of the topological insulator and corresponds to illumination by a mid-wave infrared laser with a typical spot diameter of $250 \mu\text{m}$. Using the calculated nonlinear conductivity, we obtain a responsivity of $R = 0.169 \mu\text{A}/\text{W}$ (Appendix E). As Figure 6 shows, this value is comparable to those reported experimentally for high-performance topological photodetectors [42], where other technologies require cooling. It indicates that the circular photogalvanic effect in our system can generate a measurable direct photocurrent under moderate optical excitation, demonstrating efficient light–matter coupling and potential applicability in room-temperature optoelectronic detection.

B. Eight Band Model

Several nonlinear optical experiments on $(\text{Bi},\text{Sb})_2(\text{Te},\text{Se})_3$ use visible light ($\hbar\omega \sim 1.6\text{eV}$) to generate photocurrents [16, 17, 19, 53]. At this energy range it is well established that the photocurrents are involve interband transitions between bulk states, the principal gap topological surface state and one that exists 1.6 eV higher within the conduction bands [52, 54]. In order to numerically probe the contribution of these higher energy surface state transitions, we would need to extend the tight binding model of section II to several more orbitals, which is beyond the scope of this paper. Instead, we take a phenomenological approach of creating a ‘doubled’ 8-band Hamiltonian consisting of two copies of the Bi_2Se_3 H_{tot} Hamiltonian, shifted in energy and coupled through a symmetry allowed term d

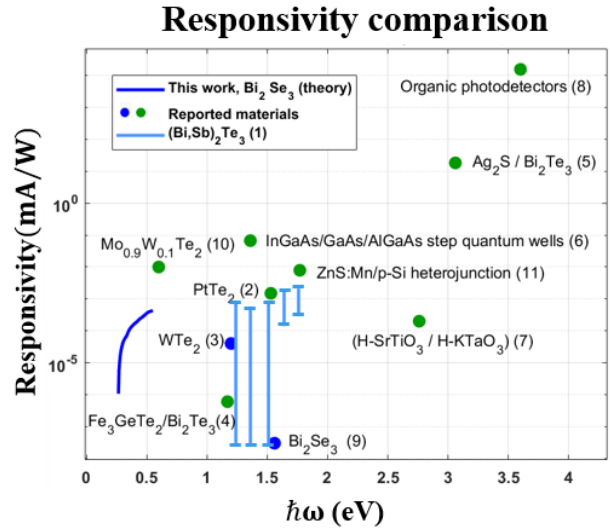


FIG. 6. Responsivity versus photon energy for a range of photodetector materials, including conventional semiconductors, topological materials, and emerging 2D systems. The responsivity calculated from Fig. 5(a) at $E_f = 0 \text{ eV}$ is shown by a dark blue line has a competitive regime relative to experimentally reported values especially at longer wavelengths (blue dots and lines represent TIs). Numbers 1-11 represent experimentally reported responsivities from Refs. [16, 42–51], respectively.

to prevent trivial crossings:

$$H_{8 \times 8}^{C_1 C_2} = \begin{pmatrix} C_1 H_{\text{tot}} & d \\ d^\dagger & 1.6 \text{ eV} + C_2 H_{\text{tot}} \end{pmatrix}, \quad (28)$$

$$d = \Gamma_2 \{ \sin(\mathbf{k} \cdot \mathbf{a}_1) + \cos(\Omega) [\sin(\mathbf{k} \cdot \mathbf{a}_2) + \sin(\mathbf{k} \cdot \mathbf{a}_3)] \}. \quad (29)$$

We've allowed for the two surface states to have opposite ($C_1 \times C_2 = -1$) or the same ($C_1 \times C_2 = 1$) chiralities. In Fig. 7(a): surface band structures of Bi_2Se_3 and $\text{Bi}_2\text{Te}_2\text{Se}$ demonstrate that at many Dirac surface states exist within the topological insulators extended conduction and valence bands, with both $+1$ and -1 chiralities [52]. In Fig. 7(b) we model band structures using Eq. (29) for both $+/+$ and $+/-$ pairings of chiralities, using pink and blue boxes to highlight surface states with $C = \pm 1$. The principal and higher conduction topological surface states of Bi_2Se_3 and Bi_2Te_3 have $+/-$ chirality pairing. Identical chirality pairs like $+/+$ are also allowed, for example the valence band and principal topological surface states in Bi_2Te_3 follow a $+/+$ pairing. The resulting calculations for σ_{xxz}^T are shown in Fig. 7(c). The chirality pairing is seen to make a significant difference in the qualitative behavior.

For the $+/-$ case, Fig. 7(c,top) the top and bottom surfaces exhibit opposite spin-momentum locking, which causes their CPGE contributions to partially cancel when integrated over the full slab. For photon energies just below the Dirac point separation, Pauli-blocking further represses the optical transitions, and the CPGE magnitude

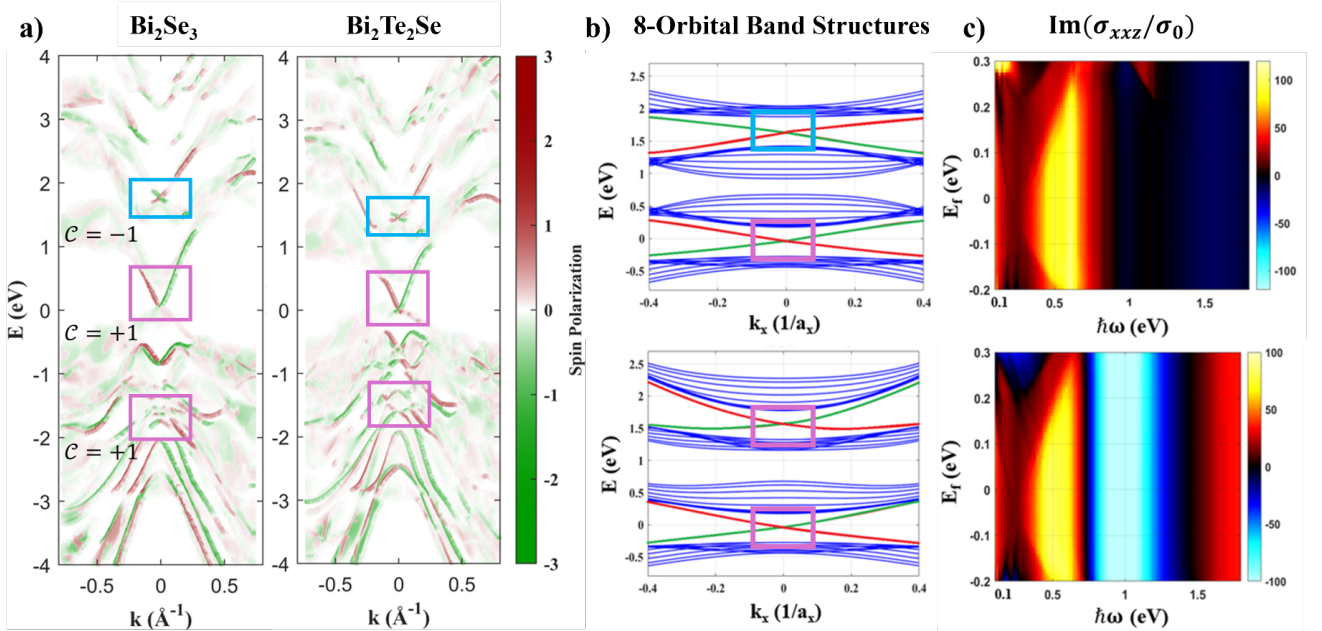


FIG. 7. a) Surface projected band structures of Bi_2Se_3 and $\text{Bi}_2\text{Te}_2\text{Se}$ using data from Ref. [52]. Multiple surface states exist in the conduction and valence bands with the same and opposite chiralities as the Dirac state in the principal gap. Pink/blue boxes highlight states of chirality $\mathcal{C} = \pm 1$ respectively. b) Simple 8-orbital band structures developed to probe the nonlinear conductivity dependence on transitions between opposite and identical chirality topological bands. c) Calculations for the top surface contribution to CPGE, $\text{Im} \sigma_{xxz}^T$, corresponding to the band structures in (b). For $+/-$ chirality pairing (top), CPGE weakens for transitions between Dirac states, and nearly vanishes due to cancellations of interband transitions between bands of opposite chirality. For $+/+$ however, CPGE magnitude remains constant across the Dirac point, with the opposite sign for $\text{Im} \sigma_{xxz}$ as in the $+/-$ case. These results demonstrate that CPGE will be enhanced by optical excitation between surface states of the same chirality, and motivates ultraviolet CPGE studies of $\text{Bi}_2\text{Te}_2\text{Se}$ to excite the surface states at ~ -1.5 eV below the intrinsic Fermi level to the Dirac states at 1.6 eV above the Fermi level in the conduction band. Note: $\sigma_0 \approx 6.85 \times 10^{-7} \text{ A/V}^2$.

decreases—consistent with wavelength dependent measurements [16]. At lower photon energies ($\hbar\omega \lesssim 0.6$ eV), the response increases again, recovering the 4-orbital model behavior when higher energy states are no longer accessible.

For the $+/+$ chirality configuration, Fig. (7)(c, bottom), both surfaces exhibit the same spin-momentum locking orientation, so their CPGE contributions add constructively, leading to an overall stronger net response. The resulting σ_{xxz}^T is more uniform and robust across a broad range of Fermi levels. Notably, the CPGE in this configuration is less sensitive to the precise position of the Fermi level relative to the Dirac point of the surface states. This behavior indicates that surfaces with matching chirality support more stable helicity-driven photocurrents, consistent with the expectation that the symmetry of spin textures governs the net CPGE response in TI slabs.

Figure 8 presents the $+/+$ configuration colormaps of σ_{xxz}^T as a function of photon energy $\hbar\omega$ for a different range, $0.5 < E_f < 2.5$ eV. By considering larger Fermi levels, we can probe the dependence on transitions between valence and principal topological bands. For photon energies greater than the Dirac point separation ($\hbar\omega > 1.6$ eV), the sign of the helicity dependence flips

as the chemical potential is tuned above and below the upper Dirac point at 1.6 eV. Pauli blocking is again manifest in diminished σ_{xxz} as photon energies dip below 1.6 eV. However, the additive nature of the $+/+$ chiralities returns for midwave infrared frequencies where robust CPGE of fixed sign persists across a large Fermi level range.

The comparison of two chirality options highlights the crucial role of surface-state chirality in determining the strength and tunability of CPGE in topological systems. Understanding and controlling the symmetry and spin texture of surface states offers a promising avenue for engineering tailored photocurrent responses in future optoelectronic and spintronic devices.

C. Magnetic Proximity Effect

The versatility of a tight binding model allows us to simulate possible engineering and device fabrication approaches to modify the nonlinear photocurrents. To investigate the influence of magnetic interactions on CPGE, we model a TI slab with a magnetic layer deposited on its surface (Fig. 3(d)). A magnetic exchange field M_z is introduced along the z -axis in the Hamilton-

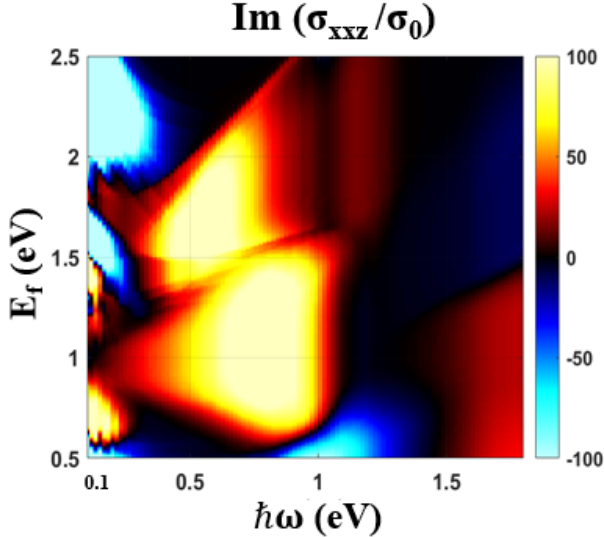


FIG. 8. Imaginary part of the second-order nonlinear optical conductivity component (σ_{xxz}^T) as a function of photon energy $\hbar\omega$ and Fermi level E_f , computed for the same $+/+$ configuration. The color map indicates a pronounced nonlinear response in regions associated with second surface state transitions and broken symmetry conditions. Note: $\sigma_0 \approx 6.85 \times 10^{-7} \text{ A/V}^2$.

nian, breaking time-reversal symmetry and opening a gap at the Dirac point of the surface-state spectrum. This magnetic gap shifts the Berry curvature from inside the gap to the region above the edges, altering the circular dichroism of the helicity-selective interband transitions.

Figure F.1 in the Appendix compares the slab band structures without and with a finite out-of-plane exchange fields. When $M_z = 0.1$, a clear gap appears at the surface Dirac point, giving rise to a massive Dirac dispersion while leaving the bulk states nearly unchanged. This behavior agrees with the low-energy surface Hamiltonian

$$H_{\text{surf}} = v_F(k_x\sigma_y - k_y\sigma_x) + M_z\sigma_z, \quad (30)$$

where the $M_z\sigma_z$ term breaks time-reversal symmetry and induces a mass gap $\Delta \propto |M_z|$ at $\mathbf{k} = 0$ [55].

Figure 9 shows the dependence of the top layers' CPGE response, $\text{Im } \sigma_{xxz}^T$, on the exchange field strength M_z at fixed Fermi energy $E_f = 0$. The $M_z = 0$ line cut is appropriately identical to the $E_f = 0$ line cut in Fig. 5(a). As M_z is increased from 0, a magnetic gap opens in the surface Dirac spectrum, shifting the onset of interband optical transitions to higher photon energies $\hbar\omega \approx 2|M_z|$. The CPGE amplitude near this threshold initially grows due to enhanced asymmetry between spin-split bands, but is subsequently suppressed as the gap widens and available low-energy transitions become Pauli-blocked. The resulting spectrum displays a distinct ridge following the linear relation between the photon energy and M_z , reflecting the magnetic control of the Dirac mass and its role in modulating the helicity-sensitive optical response.

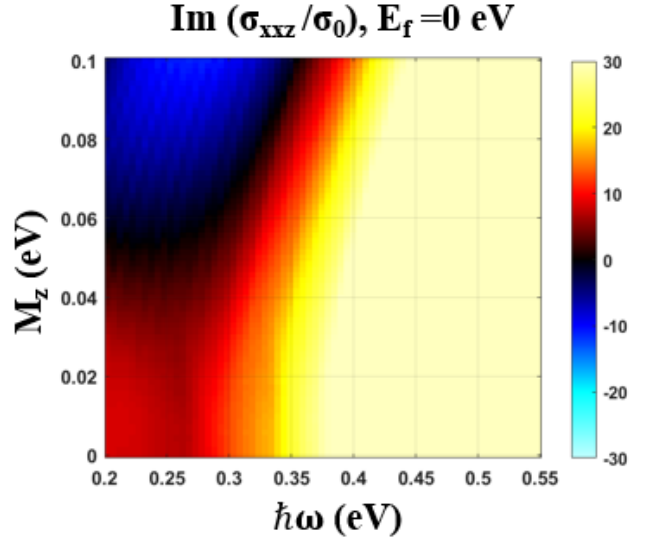


FIG. 9. color map of the imaginary part of the conductivity tensor, $\text{Im}(\sigma_{xxz}/\sigma_0)$, versus photon energy $\hbar\omega$ and out-of-plane magnetization M_z (eV) at $E_f = 0$ eV. Colors indicate the sign and magnitude of the response (red/blue for positive/negative), revealing a magnetization-dependent resonance that shifts to higher energies with increasing M_z .

In Appendix F, we further explore how for fixed top layer $M_z \neq 0$ the CPGE depends upon the Fermi level location. Figures F.2(a) and (b) show the calculated CPGE response for magnetic configuration Fig.3(d) at the top and bottom surfaces of the slab, respectively. They present surface-resolved maps of $\text{Im } \sigma_{xxz}^{(T/B)}$ with an out-of-plane exchange field M_z . Revisiting the $M_z = 0$ case calculated in Fig.5(a), a pronounced CPGE enhancement appears near the Dirac point at low photon energies, consistent with helicity-selective interband transitions of the gapless, spin-momentum-locked surface states. Introducing $M_z \neq 0$ opens a gap at the Dirac crossing and modifies the spin texture. Two main effects follow: (i) the interband absorption threshold shifts from $\hbar\omega_{\text{min}} = 0$ to $\hbar\omega_{\text{min}} \approx 2|M_z|$ for $E_f \approx 0$ due to Pauli blocking, and (ii) the surface spins acquire finite out-of-plane components, reducing the circular dichroism of the velocity matrix elements. Consequently, the low-energy CPGE is strongly suppressed within the gap window, while spectral weight accumulates just above the band edge. At higher photon energies, the response gradually recovers toward the nonmagnetic profile. In Fig. F.2(b), the bottom surface nonlinear conductivity $\text{Im } \sigma_{xxz}^B$ sees little impact of the magnetization in the top layer. It largely retains opposite CPGE signs to $\text{Im } \sigma_{xxz}^T$ for the larger photon energies, with small asymmetries arising from finite slab thickness and weak inversion breaking.

When the exchange field penetrates the entire slab (the “whole-layer” case, Fig. F.1(c), it spin-splits the bulk sub bands according to

$$E_{n\pm}(k_{\parallel}) = E_n(k_{\parallel}) \pm M_z \langle \sigma_z \rangle_n, \quad (31)$$

lifting Kramers degeneracy and reshaping the joint density of states (JDOS) [56]. The multiple interband thresholds $E_{m+} - E_{n-}$ span a wide energy range, allowing circularly polarized transitions at many photon energies. This produces the broad, smooth CPGE band observed in Fig. F.3. The uniform spin polarization also fixes the sign of $\text{Im} \sigma_{xxz}^T$ when E_f lies in the bulk gap; M_z has suppressed directional dependent spin flip transitions.

V. CONCLUSION

We employed a tight-binding slab model and the Kubo formalism to calculate the second-order nonlinear optical conductivity and photocurrent generation in TIs. Our results reveal that both the CPGE and LPGE can be effectively tuned by the Fermi level, gate voltage, photon energy, and surface magnetization. Gate-controlled inversion-symmetry breaking resonantly enhances the nonlinear optical response, particularly in the mid-infrared regime where Berry-curvature effects dominate. Both CPGE and LPGE exhibit strong voltage dependence and complementary spectral features, enabling selective enhancement of polarization-dependent photocurrents. Surface-state chirality plays a central role: opposite chiralities on the two surfaces lead to partial cancellation of CPGE contributions, whereas same-chirality configurations yield constructive interference and stronger photocurrent generation. This provides a clear strategy for symmetry and spin-texture engineering in polarization-sensitive optoelectronic systems. In addition, proximity-induced magnetization opens a tunable exchange gap in

the surface states, redistributing Berry curvature and significantly modulating the CPGE amplitude. Moderate magnetization suppresses the response within the magnetic gap, illustrating the delicate balance between time-reversal-symmetry breaking and optical excitation.

Overall, our findings demonstrate that TIs are a compelling platform for high-frequency, polarization-sensitive, and magnetically controllable, and gate/field-effect-tunable nonlinear optoelectronics. The layered simulation approach presented here enables predictive modeling of how proximate magnetic fields influence nonlinear optical processes at specific surfaces. These results provide theoretical guidance for disentangling intrinsic and extrinsic contributions to CPGE and LPGE observed experimentally and outline design principles for next-generation quantum-geometric and chiral optoelectronic devices operating from the terahertz to mid-infrared spectral range.

ACKNOWLEDGMENTS

This research was partially supported by an Industry University Cooperative Research Center provided by the Army Research Lab (ARL) and in part by the NSF I/UCRC on Multi-functional Integrated System Technology (MIST) Center; IIP-1439644, IIP-1439680, IIP-1738752, IIP-1939009, IIP-1939050, and IIP-1939012. This research was also partially supported by a Laboratory University Collaborative Initiative award provided by the Basic Research Office in the Office of the Under Secretary of Defense for Research and Engineering.

[1] J. Orenstein, J. E. Moore, T. Morimoto, D. H. Torchinsky, J. W. Harter, and D. Hsieh, Topology and symmetry of quantum materials via nonlinear optical responses, *Annu. Rev. Condens. Matter Phys.* **12**, 247 (2021).

[2] B. Keimer and J. E. Moore, The physics of quantum materials, *Nat. Phys.* **13**, 1045 (2017).

[3] F. De Juan, A. G. Grushin, T. Morimoto, and J. E. Moore, Quantized circular photogalvanic effect in weyl semimetals, *Nat. Commun.* **8**, 15995 (2017).

[4] M. Z. Hasan and C. L. Kane, Colloquium: Topological insulators, *Rev. Mod. Phys.* **82**, 3045 (2010).

[5] K. A. Kuznetsov, S. A. Tarasenko, P. M. Kovaleva, P. I. Kuznetsov, D. V. Lavrukhan, Y. G. Goncharov, A. A. Ezhov, D. S. Ponomarev, and G. K. Kitaeva, Topological insulator films for terahertz photonics, *Nanomaterials* **12**, 3779 (2022).

[6] Y. Xia, D. Qian, D. Hsieh, L. Wray, A. Pal, H. Lin, A. Bansil, D. Grauer, Y. Hor, R. Cava, *et al.*, Discovery (theoretical prediction and experimental observation) of a large-gap topological-insulator class with spin-polarized single-dirac-cone on the surface, *arXiv preprint arXiv:0908.3513* (2009).

[7] F. K. Wang, S. J. Yang, and T. Y. Zhai, 2d bi_2se_3 materials for optoelectronics, *iScience* **24**, 103203 (2021).

[8] D. Hsieh, Y. Xia, D. Qian, L. Wray, F. Meier, J. H. Dil, J. Osterwalder, L. Patthey, A. V. Fedorov, H. Lin, *et al.*, Observation of time-reversal-protected single-dirac-cone topological-insulator states in bi_2te_3 and sb_2te_3 , *Phys. Rev. Lett.* **103**, 146401 (2009).

[9] R. W. Boyd, *Nonlinear Optics (Third Edition)* (Academic Press, Burlington, 2008).

[10] M. Sheik-Bahae and M. P. Hasselbeck, Third-order optical nonlinearities, *Handbook of Optics* **4**, 16 (2000).

[11] C. Aversa and J. E. Sipe, Nonlinear optical susceptibilities of semiconductors: Results with a length-gauge analysis, *Phys. Rev. B* **52**, 14636 (1995).

[12] Y. R. Shen, *The principles of nonlinear optics*, Wiley classics library (John Wiley & Sons, 2002).

[13] T. Morimoto and N. Nagaosa, Topological nature of nonlinear optical effects in solids, *Sci. Adv.* **2**, e1501524 (2016).

[14] J. E. Sipe and A. I. Shkrebtii, Second-order optical response in semiconductors, *Phys. Rev. B* **61**, 5337 (2000).

[15] D. Hsieh, J. W. McIver, D. H. Torchinsky, D. R. Gardner, Y. S. Lee, and N. Gedik, Nonlinear optical probe of tunable surface electrons on a topological insulator, *Phys. Rev. Lett.* **106**, 057401 (2011).

[16] Y. Pan, Q.-Z. Wang, A. L. Yeats, T. Pillsbury, T. C.

Flanagan, A. Richardella, H. Zhang, D. D. Awschalom, C.-X. Liu, and N. Samarth, Helicity dependent photocurrent in electrically gated $(\text{bi}_{1-x}\text{sb}_x)_2\text{te}_3$ thin films, *Nat. Commun.* **8**, 1037 (2017).

[17] L. Braun, G. Mussler, A. Hruban, M. Konczykowski, T. Schumann, M. Wolf, M. Münzenberg, L. Perfetti, and T. Kampfrath, Ultrafast photocurrents at the surface of the three-dimensional topological insulator bi_2se_3 , *Nat. Commun.* **7**, 13259 (2016).

[18] H. Plank, J. Pernul, S. Gebert, S. N. Danilov, J. König-Otto, S. Winnerl, M. Lanius, J. Kampmeier, G. Mussler, I. Aguilera, D. Grützmacher, and S. D. Ganichev, Infrared/terahertz spectra of the photogalvanic effect in $(\text{bi}, \text{sb})\text{te}$ based three-dimensional topological insulators, *Phys. Rev. Mater.* **2**, 024202 (2018).

[19] B. C. Connelly, P. J. Taylor, and G. J. de Coster, Emergence of threefold symmetric helical photocurrents in epitaxial low twinned bi_2se_3 , *Proc. Natl. Acad. Sci. U.S.A.* **121**, e2307425121 (2024).

[20] V. I. Belinicher and B. I. Sturman, The photogalvanic effect in media lacking a center of symmetry, *Sov. Phys. Usp.* **23**, 199 (1980).

[21] V. V. Bel'kov, S. D. Ganichev, P. Schneider, C. Back, M. Oestreich, J. Rudolph, D. Hägele, L. E. Golub, W. Wegscheider, and W. Prettl, Circular photogalvanic effect at inter-band excitation in semiconductor quantum wells, *Solid State Commun.* **128**, 283 (2003).

[22] P. Hosur, Circular photogalvanic effect on topological insulator surfaces: Berry-curvature-dependent response, *Phys. Rev. B* **83**, 035309 (2011).

[23] A. Junck, G. Refael, and F. von Oppen, Photocurrent response of topological insulator surface states, *Phys. Rev. B* **88**, 075144 (2013).

[24] S. Huang and X. Xu, Optical chirality detection using a topological insulator transistor, *Adv. Opt. Mater.* **9**, 2002210 (2021).

[25] G. B. Osterhoudt, L. K. Diebel, M. J. Gray, X. Yang, J. Stanco, X. Huang, B. Shen, N. Ni, P. J. W. Moll, Y. Ran, and K. S. Burch, Colossal mid-infrared bulk photovoltaic effect in a type-i weyl semimetal, *Nat. Mater.* **18**, 471 (2019).

[26] S. Mao, A. Yamakage, and Y. Kuramoto, Tight-binding model for topological insulators: Analysis of helical surface modes over the whole brillouin zone, *Phys. Rev. B* **84**, 115413 (2011).

[27] C.-X. Liu, X.-L. Qi, H. Zhang, X. Dai, Z. Fang, and S.-C. Zhang, Model hamiltonian for topological insulators, *Phys. Rev. B* **82**, 045122 (2010).

[28] H. Zhang, C.-X. Liu, X.-L. Qi, X. Dai, Z. Fang, and S.-C. Zhang, Topological insulators in bi_2se_3 , bi_2te_3 and sb_2te_3 with a single dirac cone on the surface, *Nat. Phys.* **5**, 438 (2009).

[29] Y.-M. Xie and N. Nagaosa, Photon-drag photovoltaic effects and quantum geometric nature, *Proc. Natl. Acad. Sci. U.S.A.* **122**, e2424294122 (2025).

[30] K. Ebihara, K. Yada, A. Yamakage, and Y. Tanaka, Finite size effects of the surface states in a lattice model of topological insulator, *Physica E* **44**, 885 (2012).

[31] A. Avdoshkin, V. Kozii, and J. E. Moore, Interactions remove the quantization of the chiral photocurrent at weyl points, *Phys. Rev. Lett.* **124**, 196603 (2020).

[32] D. E. Parker, T. Morimoto, J. Orenstein, and J. E. Moore, Diagrammatic approach to nonlinear optical response with application to weyl semimetals, *Phys. Rev. B* **99**, 045121 (2019).

[33] K. Nakazawa, H. F. Legg, J. Klinovaja, and D. Loss, Interband contributions to nonlinear transport in semiconductor nanostructures, *Phys. Rev. B* **111**, 125305 (2025).

[34] H. Tanaka, H. Watanabe, and Y. Yanase, Nonlinear optical responses in noncentrosymmetric superconductors, *Phys. Rev. B* **107**, 024513 (2023).

[35] J. Han, Y. Sun, X. Huang, W. Shuai, G. Fang, and Z. Li, Design principles of nonlinear optical materials for terahertz lasers, *arXiv preprint arXiv:2402.17126* (2024).

[36] W.-X. Yu, B. Liu, W.-Q. Huang, H. Zhou, and S.-Y. Xie, Phase evolution for oxidizing bismuth selenide, *J. Phys. Condens. Matter* **35**, 075401 (2022).

[37] J. Cao, M. Wang, Z.-M. Yu, and Y. Yao, Bulk fermi arc transition induced large photogalvanic effect in weyl semimetals, *Phys. Rev. B* **106**, 125416 (2022).

[38] G. D. Mahan, *Many-Particle Physics* (Springer US, 2000).

[39] S. Dhara, E. J. Mele, and R. Agarwal, Voltage-tunable circular photogalvanic effect in silicon nanowires, *Science* **349**, 726 (2015).

[40] Y. Xia, D. Qian, D. Hsieh, L. Wray, A. Pal, H. Lin, A. Bansil, D. H. Y. S. Grauer, Y. S. Hor, R. J. Cava, et al., Observation of a large-gap topological-insulator class with a single dirac cone on the surface, *Nat. Phys.* **5**, 398 (2009).

[41] L. Fu, Hexagonal warping effects in the surface states of the topological insulator bi_2te_3 , *Phys. Rev. Lett.* **103**, 266801 (2009).

[42] X. Song, X. Liu, F. Wang, L. Du, H. Zhang, Z. Fu, W. Sun, Y. Sun, J. Zhang, Z. Dai, et al., High-responsivity vis-nir photodetectors based on bi_2te_3 thin films and ag_2s qds heterojunction, *Mater. Lett.* **377**, 137518 (2024).

[43] L. Liu, L. Du, E. Pan, X. Liu, J. Chen, L. Yu, Y. Yu, H. Zhang, X. Song, X. Yang, et al., Pt te_2 thin film photodetectors with positive photoconductivity under uv-vis-nir laser irradiation, *Chin. Opt. Lett.* **23**, 121601 (2025).

[44] S.-Y. Xu, Q. Ma, H. Shen, V. Fatemi, S. Wu, T.-R. Chang, G. Chang, A. M. M. Valdivia, C.-K. Chan, Q. D. Gibson, et al., Electrically switchable berry curvature dipole in the monolayer topological insulator wte₂, *Nat. Phys.* **14**, 900 (2018).

[45] S. You, R. Zhao, T. Nie, S. Cheng, Y. Lai, Y. Chen, J. Yu, and Z. Diao, Interface-induced 2d ferromagnetism in fe₃ge te_2 / bi_2te_3 heterostructures studied via the circular photogalvanic effect, *Applied Surface Science* **717**, 164741 (2026).

[46] J. Yu, S. Cheng, Y. Lai, Q. Zheng, and Y. Chen, Spin photocurrent spectra induced by rashba- and dresselhaus-type circular photogalvanic effect at interband excitation in ingaas/gaas/algaas step quantum wells, *Nanoscale Res. Lett.* **9**, 130 (2014).

[47] C. Li, Y. Li, G. Li, and J. Guo, Circular photogalvanic effect at the surface of hydrogenated perovskite oxides, *Appl. Phys. Lett.* **126**, 251101 (2025).

[48] L. Liu, Y. Yang, L. Zhu, J. Zhang, K. Chen, and Z. Wei, Chiral non-fullerene acceptor enriched bulk heterojunctions enable high-performance near-infrared circularly polarized light detection, *Small* **18**, 2202941 (2022).

[49] J. W. McIver, D. Hsieh, H. Steinberg, P. Jarillo-Herrero, and N. Gedik, Control over topological insulator photocurrents with light polarization, *Nat. Nanotechnol.* **7**,

96 (2012).

[50] Z. Ji, G. Liu, Z. Addison, W. Liu, P. Yu, H. Gao, Z. Liu, A. M. Rappe, C. L. Kane, E. J. Mele, et al., Spatially dispersive circular photogalvanic effect in a weyl semimetal, *Nat. Mater.* **18**, 955 (2019).

[51] A. Kumar, S. Mukherjee, H. Sharma, D. K. Rana, A. Kumar, R. Kumar, and R. K. Choubey, Fabrication of low-cost and fast-response visible photodetector based on zns:mn/p-si heterojunction, *Mater. Sci. Semicond. Process.* **155**, 107226 (2023).

[52] I. Aguilera, C. Friedrich, and S. Blügel, Many-body corrected tight-binding hamiltonians for an accurate quasiparticle description of topological insulators of the Bi_2Se_3 family, *Phys. Rev. B* **100**, 155147 (2019).

[53] C.-M. Tu, Y.-C. Chen, P. Huang, P.-Y. Chuang, M.-Y. Lin, C.-M. Cheng, J.-Y. Lin, J.-Y. Juang, K.-H. Wu, J.-C. A. Huang, W.-F. Pong, T. Kobayashi, and C.-W. Luo, Helicity-dependent terahertz emission spectroscopy of topological insulator Sb_2Te_3 thin films, *Phys. Rev. B* **96**, 195407 (2017).

[54] J. A. Sobota, S. Yang, J. G. Analytis, Y. L. Chen, I. R. Fisher, P. S. Kirchmann, and Z.-X. Shen, Ultrafast optical excitation of a persistent surface-state population in the topological insulator Bi_2Se_3 , *Phys. Rev. Lett.* **108**, 117403 (2012).

[55] X.-L. Qi and S.-C. Zhang, Topological insulators and superconductors, *Rev. Mod. Phys.* **83**, 1057 (2011).

[56] V. I. Litvinov, Magnetic exchange interaction in topological insulators, *Phys. Rev. B* **89**, 235316 (2014).